INTERNATIONAL JOURNAL FOR NUMERICAL METHODS IN FLUIDS
Int. J. Numer. Meth. Fluids 2009; **59**:1285–1298
Published online 14 July 2008 in Wiley InterScience (www.interscience.wiley.com). DOI: 10.1002/fld.1872

3D numerical simulation of compressible swirling flow induced by means of tangential inlets

Hui-Fen Guo[1], Zhi-Yong Chen[2] and Chong-Wen Yu[1, 3, *, †]

[1]*Textile College, Dong Hua University, Shanghai 201620, People's Republic of China*
[2]*Shanghai Institute of Applied Mathematics and Mechanics, Shanghai University, Shanghai 200072, People's Republic of China*
[3]*The Key Lab of Textile Science & Technology Ministry of Education, Dong Hua University, Shanghai 201620, People's Republic of China*

SUMMARY

The objective of the present work is to predict compressible swirl flow in the nozzle of air-jet spinning using the realizable k–ε turbulence model and discuss the effect of the nozzle pressure. The periodic change of flow patterns can be observed. The recirculation zone near the wall of the injectors upstream increases in size and moves gradually upstream, whereas the vortex breakdown in the injector downstream shifts slowly towards the nozzle outlet during the whole period. A low axial velocity in the core region moves gradually away from the centerline, and the magnitude of the center reverse flow and the area occupied by it increase with axial distance due to the vortex breakdown. From the tangential velocity profile, there is a very small free-vortex zone. With increasing nozzle pressure, the velocity increases and the location of vortex breakdown is moved slightly downward. However, the increase in the velocity tends to decline at nozzle pressure up to a high level. Copyright © 2008 John Wiley & Sons, Ltd.

Received 4 March 2008; Revised 23 May 2008; Accepted 27 May 2008

KEY WORDS: swirling flow; vortex breakdown; reverse flow; recirculation zone; turbulence; nozzle

1. INTRODUCTION

Turbulent swirling decaying flow in the nozzle of air-jet spinning plays an important role in influencing fiber motion and therefore the quality of the yarn. Consequently, increased attention is being paid to the prediction of the swirling flow characteristics in the twisting chamber in order to

*Correspondence to: Chong-Wen Yu, Textile College of Donghua University, No. 2999, Renming North Road, Daxuecheng of Songjiang, Shanghai 201620, People's Republic of China.
†E-mail: yucw@dhu.edu.cn

Contract/grant sponsor: Specialized Research Fund for the Doctoral Program of Higher Education; contract/grant number: 20040255009

produce a high quality yarn. However, at present, most of the information available in the literature on air-jet spinning is related to the yarn structure [1–3], the principle of yarn formation [1, 4] and the effects of various parameters on yarn quality [1–3, 5, 6], and these are closely related to the flow characteristics in the nozzle. Only Zeng and Yu [6] and Yu and Zhang [7] used experimental and numerical methods, respectively, to study 2D airflow field in the nozzle. This cannot show some important properties of the swirling flow because this flow is very complex and exhibits a strong three-dimensional behavior characterized by curved streamlines [8]. Therefore, the present work is to systematically study 3D swirl flow characteristics in the nozzle of air-jet spinning.

In air-jet spinning, the swirl flow in the nozzle is created by injecting tangentially high-velocity compressed air through evenly spaced injectors placed on the periphery of the twisting chamber (tube). Several experimental studies of turbulent tubular swirl flows induced by tangential inlets have also been reported in the literature [9–13]. The first experimental study in this area was done by Nissan and Bresan [9]. In their work, profiles of the static pressure along the radius of the tube always showed a minimum at the center, with a steady increase towards the wall. The tangential velocity profile showed the velocity to increase from zero at the center to a maximum at a radius usually less than half the tube radius and to decrease again to zero at the wall.

Ito *et al.* [10] experimentally investigated the decay of swirl using water as the test fluid. The ratio of tangential to axial momentum flux was approximately 50. It was shown that the axial velocity was lower in the middle portion of the tube than that near the wall. The radial velocity was much smaller than the axial and tangential velocities, such that it could be ignored, and the swirl intensity was found to decay exponentially with axial distance. All these results coincide with the observation indicated by Chang and Dhir [11], who experimentally studied turbulent swirl flow in a tube by using four and six tangential inlets, and air was used as the test fluid.

Numerical simulation of swirling flows is a very important tool to assist in experiments and to gain deep understanding of the fundamental flow physics, since the experiments are often limited due to practical reasons that only a few discrete positions and not a whole 3D structure can be provided. Several authors have applied conventional Reynolds-averaged-Navier–Stokes (RANS) models to simulate pipe swirling flows induced by a tangential inlet [14–17]. It is well known that the nature of swirling itself causes considerable degree of anisotropy in stress and dissipation tensors leading to a highly anisotropic eddy viscosity according to the works of Yajnik and Subbsish [12] and Kitoh [13]. Thus, the classical k–ε model, which is the eddy-viscosity-based model, is not expected to give reliable results. Kobayashi and Yoda [16] attempted to simulate swirling flow in a pipe by using the k–ε model. They indicated that the obtained velocity profiles are quite different from the experimental data and concluded that eddy viscosity components are anisotropic. They obtained satisfactory results by considering an anisotropic factor for eddy viscosity with a modified k–ε model. Najafi *et al.* [17] simulated the turbulent swirling decay pipe flow and compared their results with the existing experimental data. They also showed that the RSM model is generally more reliable than the two-equation models. However, the RSM model requires a large amount of memory and computing time and it may be difficult to obtain a convergent solution.

At present, most published research on swirl flow is related to an incompressible fluid. However, in the nozzle of air-jet spinning, compressibility cannot be ignored due to high-velocity jet through very small orifices. Therefore, in this paper a 3D compressible realizable k–ε turbulence model is adopted to simulate the swirl flow in the nozzle of air-jet spinning. Since the nozzle pressure is the most important parameter in air-jet spinning, its effect on fluid flow is also discussed.

DOI: 10.1002/fld

2. THEORETICAL BASIS

2.1. Nozzle structure

Ignoring the influence of the fibers or strands, airflow in the nozzle will be a classical fluid flow problem. Normally the nozzle is made cylindrical in shape in the spinning process. Figure 1 shows the profiles used in the 3D simulation. In this research, the computational domain is the twisting chamber of the nozzle from the inlet to the outlet, including the injectors. A 3D Cartesian coordinate system as illustrated in Figure 1 is used. The origin of the coordinates system is located at the center of the nozzle inlet. The z-axis is taken as the streamwise direction and the x–y plane is perpendicular to the z-axis (i.e. the nozzle inlet). The twisting chamber diameter D is 2 mm, the jet length L is 25 mm, the diameter of the injector d is 0.45 mm, the injection angle θ is 45° and the position of the injector l, which is the distance from the injector to the outlet, is 14 mm.

2.2. Governing equations and turbulence model

Since high-velocity compressed air is forced into the twisting chamber through the injectors from the air reservoirs, its Mach number is large (in the range of 0.6–0.9) [7], compressibility effects are important. In our simulation, the air entering the twisting chamber is modeled as an ideal gas in the absence of body forces. The fluid viscosity, the specific heat capacity and thermal conductivity are assumed to be constant. Therefore, Favre-averaged mean equations [18] of continuity, the motion equation, the energy equation and the equation of state in Cartesian tensor notation can be written as follows:

$$\frac{\partial \overline{\rho}}{\partial t}+\frac{\partial}{\partial x_i}(\overline{\rho}\widetilde{u}_i)=0 \tag{1}$$

$$\frac{\partial}{\partial t}(\overline{\rho}\widetilde{u}_i)+\frac{\partial}{\partial x_j}(\overline{\rho}\widetilde{u}_i\widetilde{u}_j)=-\frac{\partial \overline{p}}{\partial x_i}+\frac{\partial}{\partial x_j}(\widetilde{\tau}_{ij}-\overline{\rho u_i'' u_j''}) \tag{2}$$

$$\frac{\partial}{\partial t}(\overline{\rho}\widetilde{e}_0)+\frac{\partial}{\partial x_j}(\overline{\rho}\widetilde{u}_j\widetilde{e}_0)=-\frac{\partial}{\partial x_j}\left[\widetilde{u}_j\overline{p}+\widetilde{u}_i(\overline{\rho u_i'' u_j''}-\widetilde{\tau}_{ij})+C_p\left(\overline{\rho u_j'' T}-\frac{\mu}{Pr}\frac{\partial \widetilde{T}}{\partial x_j}\right)\right] \tag{3}$$

$$\overline{p}=\overline{\rho}(\gamma-1)\left(\widetilde{e}_0-\frac{\widetilde{u}_k\widetilde{u}_k}{2}-k\right) \tag{4}$$

where an overbar indicates the mean with Reynolds averaging. A tilde and a double prime are the corresponding mean for Favre averaging. In addition, x_i $(i=1,2,3)$ are the coordinate directions, and u_i are the velocities in the three coordinates directions. ρ, p, T, μ and Pr are the air density, pressure, temperature, laminar viscosity and Prandtl number, respectively. k defined by $\overline{\rho}k=\frac{1}{2}\overline{\rho u_i'' u_i''}$ is the turbulence kinetic energy, $\widetilde{e}_0\equiv C_v\widetilde{T}+\frac{1}{2}\widetilde{u}_i\widetilde{u}_i+k$ is the mean total energy and γ is the ratio of specific heats (C_p/C_v, where C_p and C_v are specific heat capacity and constant volume specific heat, respectively). $\widetilde{\tau}_{ij}=\mu(\partial\widetilde{u}_i/\partial x_j+\partial\widetilde{u}_j/\partial x_i-\frac{2}{3}(\partial\widetilde{u}_k/\partial x_k)\delta_{ij})$ is the mean viscous stress tensor, where δ_{ij} is the Kronecker delta.

The mean conservation equations have resulted in additional terms: the Favre-averaged Reynolds stress tensor ($\tau_{ij}^{\text{turb}}\equiv-\overline{\rho u_i'' u_j''}$) and turbulent heat flux ($q_j^{\text{turb}}\equiv C_p\overline{\rho u_j'' T}$). They can be modeled using

DOI: 10.1002/fld

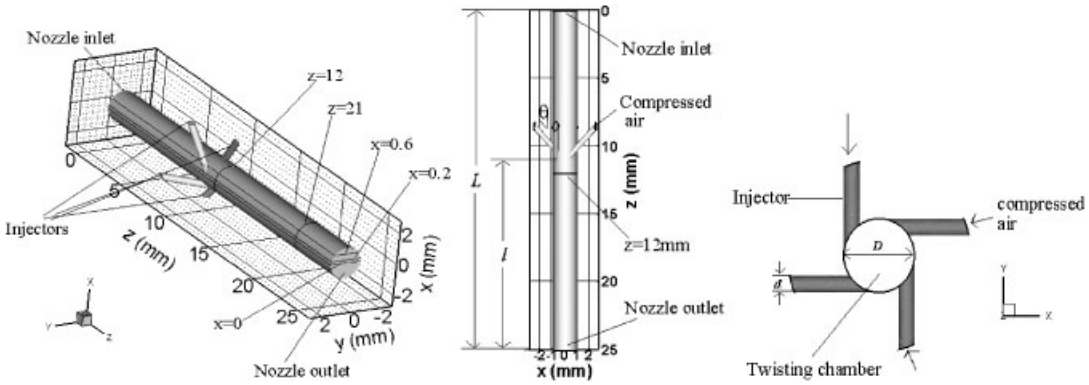

Figure 1. Profiles of a 3D model and projections of the nozzle.

an eddy viscosity assumption for the Reynolds stresses and a gradient-diffusion approximation for the turbulent heat flux:

$$\tau_{ij}^{\text{turb}} = \mu_{\text{t}} \left(\frac{\partial \widetilde{u}_i}{\partial x_j} + \frac{\partial \widetilde{u}_j}{\partial x_i} - \frac{2}{3} \frac{\partial \widetilde{u}_k}{\partial x_k} \delta_{ij} \right) - \frac{2}{3} \overline{\rho} k \delta_{ij} \tag{5}$$

$$q_j^{\text{turb}} = -C_p \frac{\mu_{\text{t}}}{Pr_{\text{t}}} \frac{\partial \widetilde{T}}{\partial x_j} \tag{6}$$

where μ_{t} is a turbulent viscosity and $Pr_{\text{t}} = 0.9$ is a turbulent Prandtl number.

The standard k–ε two-equation turbulence model has been widely applied to engineering practice, but has been criticized as being only qualitatively correct in the simulation of confined swirling flows [19–23]. This is because of the neglect of anisotropic eddy viscosity and additional turbulence generation arising from the effects of streamline curvature in the standard k–ε model [20, 24]. The realizable k–ε model belongs to the k–ε family of turbulence models; however, unlike the standard k–ε model, the realizable k–ε turbulence model, which was proposed by Shih *et al.* [25], satisfies certain mathematical constraints on the Reynolds stresses, consistent with the physics of turbulent flows. This model consists of a new model dissipation rate equation and a new realizable eddy viscosity formulation. The realizable k–ε model has shown substantial improvements on the standard k–ε model where the flow features include strong streamline curvature, vortices and recirculation [25–27]. Hence, it is adopted to close Favre-averaged equations in this paper. The modeled transport equations for k and ε in the realizable k–ε model are given as follows:

$$\frac{\partial \overline{\rho} k}{\partial t} + \frac{\partial}{\partial x_i} (\overline{\rho} \widetilde{u}_j k) = \frac{\partial}{\partial x_i} \left[\left(\mu + \frac{\mu_{\text{t}}}{\sigma_k} \right) \frac{\partial k}{\partial x_j} \right] + G_k - \overline{\rho} \varepsilon - Y_M \tag{7}$$

and

$$\frac{\partial (\overline{\rho} \varepsilon)}{\partial t} + \frac{\partial}{\partial x_i} (\overline{\rho} \widetilde{u}_j \varepsilon) = \frac{\partial}{\partial x_i} \left[\left(\mu + \frac{\mu_{\text{t}}}{\sigma_\varepsilon} \right) \frac{\partial \varepsilon}{\partial x_j} \right] + \overline{\rho} C_1 S \varepsilon - \overline{\rho} C_2 \frac{\varepsilon^2}{k + \sqrt{v\varepsilon}} \tag{8}$$

where $C_1 = \max[0.43, \eta/(\eta+5)]$ and $\eta = Sk/\varepsilon$.

DOI: 10.1002/fld

In these equations, S is the mean rate-of-strain tensor ($S \equiv \sqrt{2S_{ij}S_{ij}}$, where $S_{ij} = \frac{1}{2}(\partial u_j/\partial x_i + \partial u_i/\partial x_j)$), G_k represents the generation of turbulence kinetic energy due to the mean velocity gradients. Y_M is the contribution of the fluctuating dilatation in compressible turbulence to the overall dissipation rate. σ_k and σ_ε are the turbulent Prandtl numbers for k and ε, respectively.

Another main feature of the realizable k–ε model is that the variable C_μ in the eddy viscosity formula is a function of mean strain and rotation rates, the angular velocity of the system rotation, and the turbulence fields (k and ε). It can be computed from [28]

$$C_\mu = \frac{1}{A_0 + A_s kU^*/\varepsilon} \tag{9}$$

where $U^* = \sqrt{S_{ij}S_{ij} + \widetilde{\Omega}_{ij}\widetilde{\Omega}_{ij}}$ in which $\widetilde{\Omega}_{ij} = \Omega_{ij} - 2\varepsilon_{ijk}\omega_k$ and $\Omega_{ij} = \overline{\Omega_{ij}} - \varepsilon_{ijk}\omega_k$ where $\overline{\Omega_{ij}}$ is the mean rate-of-rotation tensor, and ε_{ijk} is the alternation tensor. The model constants A_0 and A_s are given by $A_0 = 4.04$, $A_s = \sqrt{6}\cos\phi$, $\phi = \frac{1}{3}\cos^{-1}(\sqrt{6}W)$, $W = S_{ij}S_{jk}S_{ki}/\widetilde{S}$, $\widetilde{S} = \sqrt{S_{ij}S_{ij}}$.

The constants used in this model are defined [25]: $C_2 = 1.9$, $\sigma_k = 1.0$, $\sigma_\varepsilon = 1.2$.

2.3. Boundary conditions

The inlet boundary: The airflow in the nozzle is a more complex flow with multiple inlets and different conditions. Because the pressure of the air reservoir is known, pressure inlet condition is used at the injector inlets. However, at the nozzle inlet, while the fibers or strands output from the front roller and go into the nozzle, the outer air is supplied into the nozzle; hence, velocity inlet boundary can be set.

The outlet boundary: At the nozzle outlet, the pressure is supposed to be the external pressure.

The wall boundary: At wall, non-slip boundary condition is applied.

2.4. Numerical method

To solve the governing equations, the finite-volume scheme based on the FLUENT code is employed. Owing to compressible effects, the coupled implicit approach is adopted. It performs a simultaneous solution of the conservation of mass, momentum, energy, turbulent kinetic energy and its dissipation rate equations within the physical domain. The conservation equations are solved using the second-order upwind (SOU) scheme, and the other (k and ε) equations use the quadratic upstream interpolation of convective kinematics (QUICK) scheme [29], which provides high accuracy for swirling flows.

In order to accelerate the convergence of the solver, a block Gauss–Seidel algorithm is used in conjunction with an algebraic multigrid (AMG) method [30–32] to solve the discretized equations. AMG is a method for solving matrix equations, which is based on multigrid concepts that effectively reduce the distribution of low-frequency errors. It is relatively economical on computer storage and CPU time, both scaling linearly with problem size. In the AMG methods, the coarse grid points and restriction and interpolation operators are constructed by considering only the linear system and the coupling between the different unknowns. The defect in any coarse level cell is given by the sum of those from the fine level cells it contains, whereas fine level corrections are obtained by injection of coarse level values [30, 33, 34]. Therefore, the AMG method has the advantage that no coarse level grids have to be generated or stored, and no fluxes or source terms need be calculated on the coarse levels. This feature makes AMG particularly important for use on unstructured meshes.

DOI: 10.1002/fld

Convergence was judged not only by examining the scaled residual values (i.e. residual is normalized by the respective the largest absolute value of the residual in the first five iterations) for all solution variables but also by monitoring the average value of mass flow rate on $z = 12\,\text{mm}$ surface. The solution convergence is obtained as the average mass-flow-rate value stops changing. In addition, the mass fluxes through $z = 12\,\text{mm}$ surface is checked to ensure that mass is being conserved, i.e. the ratio of the net mass imbalance to the total flux through the system is below 0.8%.

3. RESULTS AND DISCUSSION

3.1. Validation of the numerical code and grid independency

Owing to the sharp-pointed angles located in the intersection between the injectors and the twisting chamber, a regular mesh is difficult to apply in the entire geometry. A hybrid non-uniform grid is generated (Figure 2). To prove grid independency, three different grids with 134 140 (Grid 1), 198 851 (Grid 2) and 252 923 (Grid 3) cells have been tested. In all cases, grid refinements in the regions of expected high gradients, e.g. near the wall and at the zone corresponding to the intersection volume between the injectors and the twisting chamber, are applied. As shown in Figure 3, all three grids predict very similar velocity profiles. Therefore, the mesh employed will be deemed to be satisfactory and further refinements of the mesh will not be beneficial. Considering the computational effort, Grid 2 is preferred. In the following analysis, computational results are obtained using Grid 2.

In order to test the accuracy of our numerical method, the computed axial and tangential velocities with the realizable k–ε model are compared with the experimental results of Yu and Zhang [7]. The results are shown in Figure 3. Owing to the limitation of experimental conditions, Yu and Zhang measured only the velocities at the injector and nozzle outlets under the Reynolds similarity (the model is 5 times as large as the prototype). It can be observed from the figures that

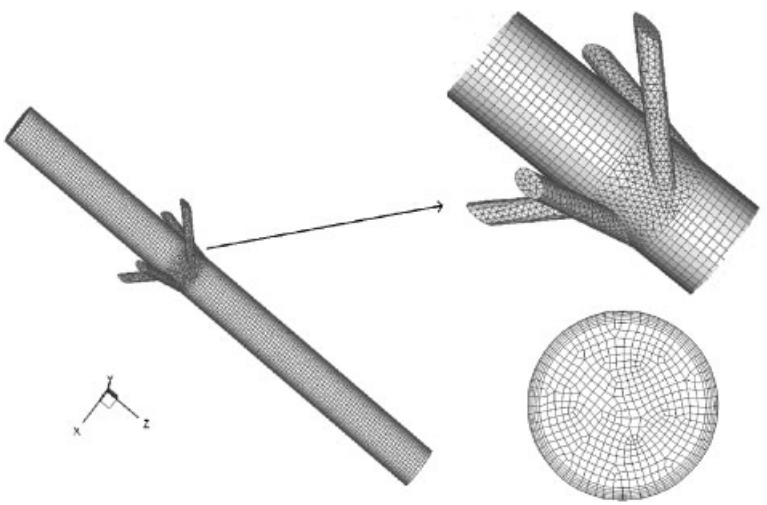

Figure 2. Mesh topology of the nozzle.

DOI: 10.1002/fld

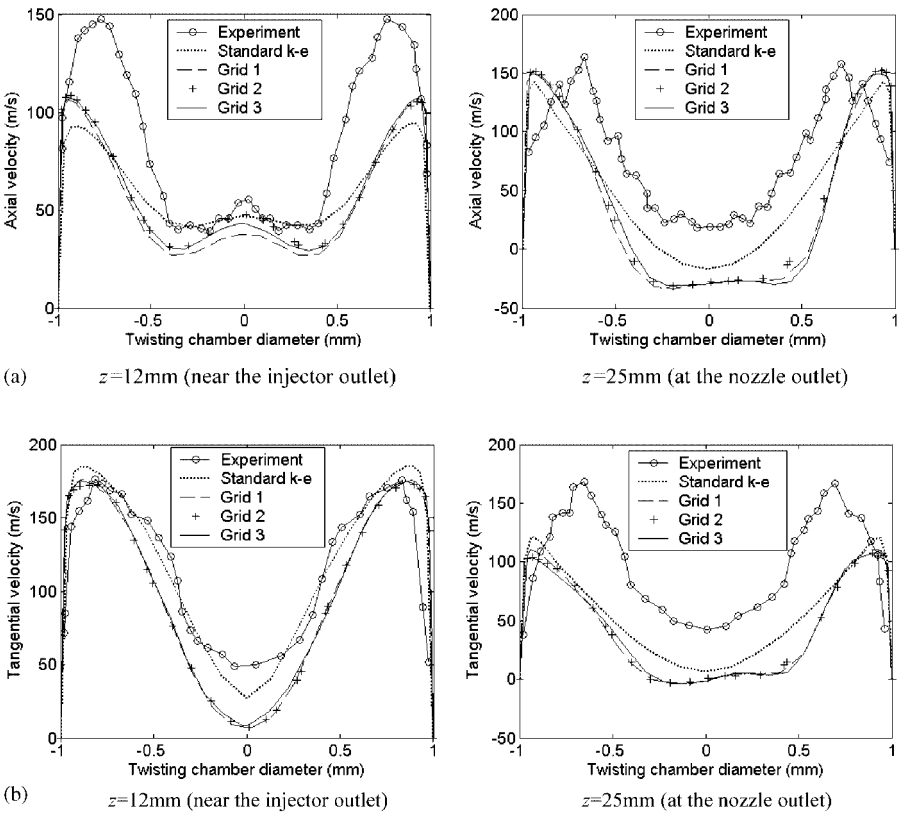

Figure 3. Comparison of the computed axial and tangential velocities' profiles at different axial locations with the experimental results of Yu and Zhang [7]: (a) axial velocities and (b) tangential velocities.

the model predictions differ from the experimental results in the quantitative sense. The model predicts lower velocity, a smaller near-wall zone and a larger center zone. The difference between numerical simulation and experiment can be attributed to the variation in inlet conditions, as the supplement of air through the nozzle inlet is ignored in the measure. Corresponding to the theory analysis [7] and simulation results, the equality of Mach numbers for the prototype and the model is paramount because Mach numbers near the injector outlet is close to 1.0 (see also Figure 6). Therefore, the other probable reason that causes the difference between simulation and experiment is that the Reynolds similarity is used in the measurement. However, in a qualitative sense, the model predicts the velocity distributions quite well, as seen from the figures.

The predicted results of the standard k–ε model are also presented in Figure 3 to assess the merits of the realizable k–ε model. In contrast with the results of the measurements and realizable k–ε model, near the wall, the standard k–ε model predicted a lower axial velocity and higher tangential velocity except at the nozzle outlet. However, in the central region, its velocity distributions are sharper and, consequently, both the strength and area of the vortex breakdown become smaller than those of the realizable k–ε model. This is a major difference between the two turbulence models' predictions. It appears that the results given by the realizable k–ε model are in better agreement

DOI: 10.1002/fld

with experimental data than the standard k–ε model. This may be due to the fact that the realizable k–ε model includes the effects of mean rotation in the definition of the turbulent viscosity (see Equation (9)).

3.2. *Flow structure*

A series of time evolution flow structures with the computed streamlines show a periodical behavior (Figure 4). The general flow structure in Figure 4(l) is similar to that in Figure 4(a), which indicates the beginning of a new period. In the upstream of the injectors, an interface between the inflow from the nozzle inlet and reverse-jet airflow of the injector is formed (Figure 4(b)–(j)), and the location of the interface moves upstream gradually and finally reaches near the nozzle inlet (Figure 4(b)–(f)); thereafter, it shifts towards the injector again slowly (Figure 4(f)–(j)). On the other hand, the recirculation zones near the wall in the injector upstream are generated, and its location shifts towards the nozzle inlet (Figure 4(a)–(l)). In the injector downstream, spiral-type vortex breakdown is generated. The flow in the breakdown region periodically rotates around the centerline (z-axis), and a period is shown in Figure 4(a)–(e). In comparison with Figure 4(a) the flow field looks like turned around the centerline about 180° at the semiperiod in Figure 4(c), where the breakdown point moves downstream slightly. First in Figure 4(a), there is a counterclockwise vortex below the centerline. On the other side of the centerline, there are two clockwise rotating vortices on the left and right sides of the lower vortex. The gross vortex distribution moves downstream, and the upper right vortex begins to slowly move out of the twisting chamber (Figure 4(b)). At the same time, a new counterclockwise vorticity field near the breakdown point begins to grow below the centerline (Figure 4(b)–(c)). The same process takes place below the centerline with a reversed sign of vorticity (Figure 4(d)–(e)). Similar results were observed by Brücker [35]. Note that the location of the stagnation point shifts slowly towards the nozzle outlet during the whole developing period. According to these results, it can be inferred that vortex breakdown will disappear after a long enough time.

Based on the above analysis, the duration of one period is very short (about 1.1×10^{-4} s). In fact, the air vortex in the nozzle rotates at a very high rate (about two to three million r/min) and the fiber bundle rotates at 200 000–300 000 r/min [36]. Therefore, the twisting process will occur in a very short time. To save computed cost, the following study will be completed under steady-state assumption.

The streamline plots at different sections are shown in Figure 5. A strong, large-scale swirling flow is observed at the two cross sections (Figure 5(a)–(b)). The center of the large swirling flow, marked in the figure with a '+' sign, is generally on the twisting chamber axis (centerline) near the injection location. However, it departs gradually from the axis further downstream of the injectors due to the occurrence of asymmetric spiral breakdown [35]. This leads to a non-zero radial and tangential velocity component at the z-axis, see also Figure 7. As shown in Figure 5(c), in the injectors upstream, reverse flow appears near the wall due to reverse jet. Therefore, a weak balloon is formed here and its rotation direction is opposite to that of both the injector downstream and the core zone of the injector upstream (Figure 5(d)–(e)). At a distance of about 7 mm (*viz.*, $z = 18$ mm) downstream of the injectors, the streamlines in the near axis core region show flow reversals, i.e. internal recirculation zones (IRZ) are generated as a result of the vortex breakdown, see also Figure 5(c). The IRZ is of spiral type, whose shape is not axisymmetric. The spiral structure obtained (Figure 5(c)) agrees well with the experimental results presented by Brücker [35]. As also observed experimentally [35, 37], the sense of the spiral's winding is opposite to the sense of basic

DOI: 10.1002/fld

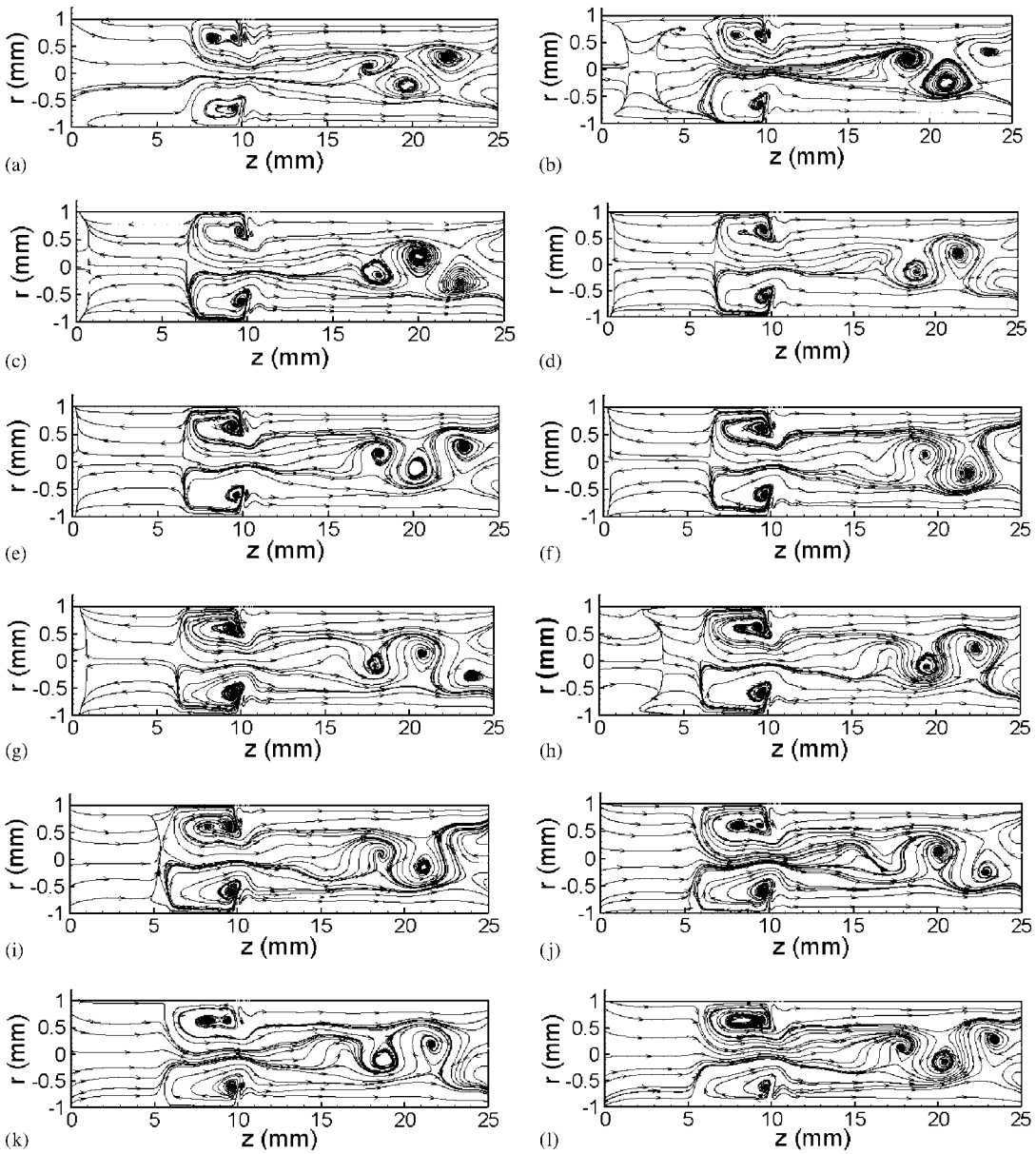

Figure 4. Time series of the streamlines in the y–z plane at $x = 0$ mm: (a) $t = 0$ s; (b) $t = 1.0 \times 10^{-5}$ s; (c) $t = 2.0 \times 10^{-5}$ s; (d) $t = 3.0 \times 10^{-5}$ s; (e) $t = 4.0 \times 10^{-5}$ s; (f) $t = 5.0 \times 10^{-5}$ s; (g) $t = 6.0 \times 10^{-5}$ s; (h) $t = 7.0 \times 10^{-5}$ s; (i) $t = 8.0 \times 10^{-5}$ s; (j) $t = 9.0 \times 10^{-5}$ s; (k) $t = 1.0 \times 10^{-4}$ s; and (l) $t = 1.1 \times 10^{-4}$ s.

DOI: 10.1002/fld

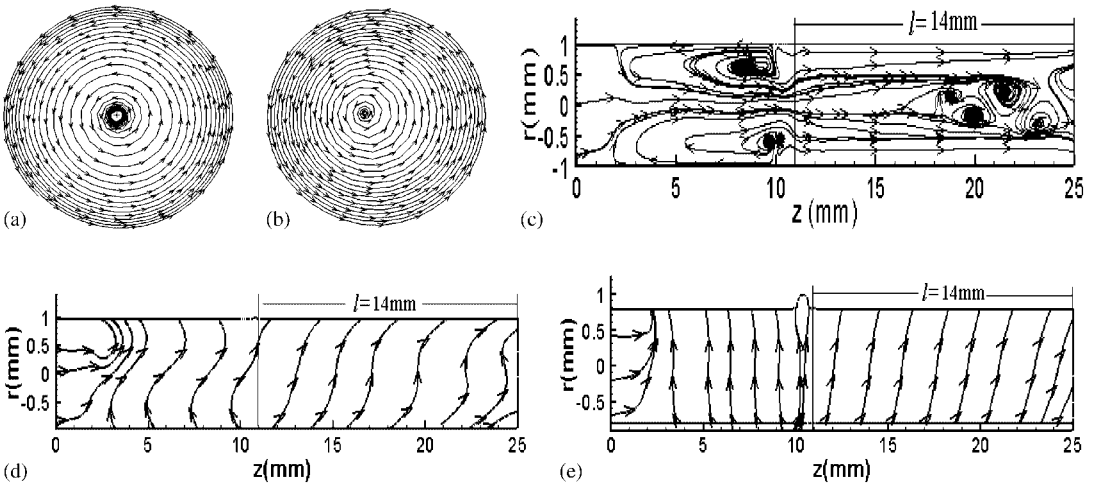

Figure 5. Predicted streamline plots at different sections: (a) the x–y plane at $z=12$ mm; (b) the x–y plane at $z=21$ mm; (c) the y–z plane at $x=0$ mm; (d) the y–z plane at $x=0.2$ mm; and (e) the y–z plane at $x=0.6$ mm.

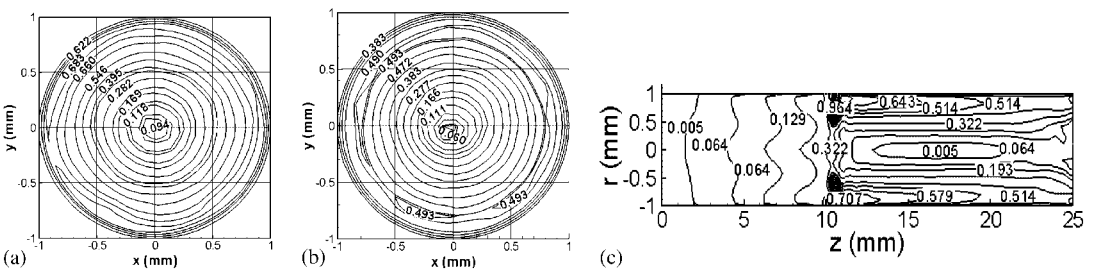

Figure 6. Contour plots of Mach number at different sections: (a) the x–y plane at $z=12$ mm; (b) the x–y plane at $z=21$ mm; and (c) the y–z plane at $x=0$ mm.

flow rotation (Figure 5(c)–(e)) and the spiral breakdown became turbulent after a few turns of the spiral. On the other hand, expansion of the vortex core downstream of the breakdown leaves very little space near the periphery for the air to flow, resulting in a higher stream velocity (Figure 7).

Mach number is the most important similarity parameter in the compressible fluid. It controls the characteristics of the compressible flow and indicates compressible degree. Figure 6 shows that Mach number is the smallest in the center zone, and it is symmetric near the injector ($z=12$ mm). However, the smallest Mach number departs from the center zone further downstream of the injector ($z=21$ mm) due to the occurrence of the vortex breakdown. The Mach number is less than (approaches) 1.0 near the injector outlets. Hence, compressibility effects are important and the flow is subsonic in the twisting chamber. This agrees with the theory analysis by Yu and Zhang [7].

Figure 7 shows the three velocity components profiles along the radial direction at different axial locations. The tangential velocity is the largest of the three components of velocity vector. According to studies on swirling flows [10, 11, 38], the radial velocity is the weakest component

DOI: 10.1002/fld

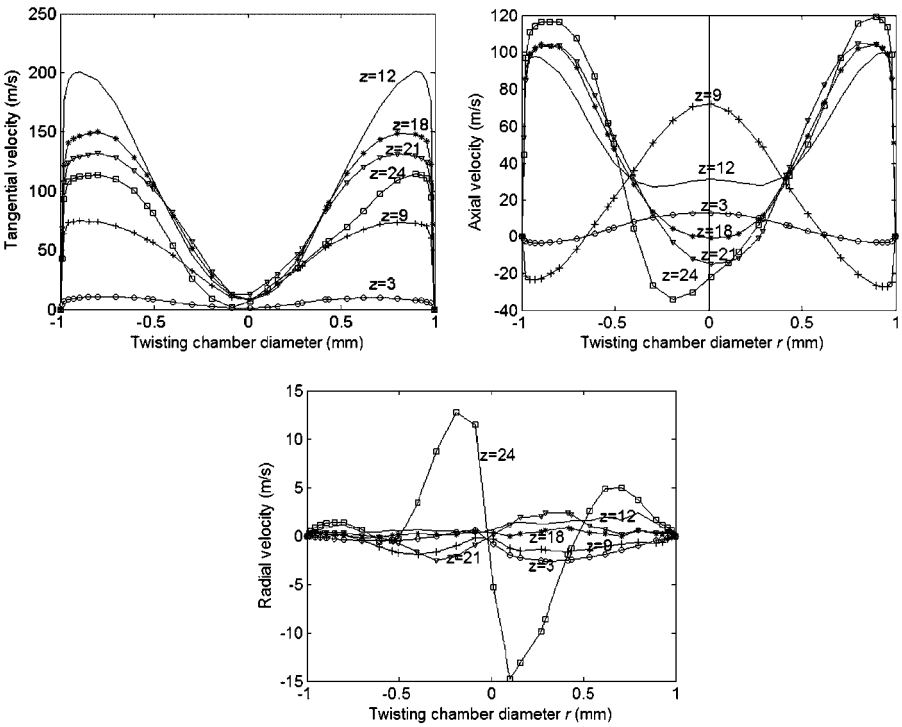

Figure 7. Three velocity components along the radial direction at different z-axial positions.

and it can be ignored. In upstream of the injector, the distributions of three velocity components are axisymmetric. However, in downstream of the injectors, the lowest axial and tangential velocities begin gradually to depart from the centerline with axial distance due to the vortex breakdown. In addition, the maxima of both tangential and axial velocities are located near the wall, and they shift towards the center of the twisting chamber before the vortex breakdown; thereafter, they shift towards the wall. This is because the effects of both the centrifugal force and the vortex breakdown, which is induced by the tangential inlet. By identifying the location at which the maximum tangential velocity occurs, the tangential velocity profile can be divided into two regions—the core (forced-vortex) and annular (free-vortex) regions. This is in agreement with other works dedicated to swirl motion using incompressible fluid [9–11]. However, under compressible condition, there is a very small free-vortex zone and a little large transition zone between the forced-vortex zone and the free-vortex zone. For the axial velocity distribution, a flow-reversal region appears at the center, and the magnitude of the reverse flow and the area occupied by it increase with axial distance due to vortex breakdown. This contradicts the experimental results by Chang and Dhir (incompressible air was used as the test fluid) [11], owing to the compressibility effects. It is clear from the figures that a change in the distribution of axial velocity is from a jet-like profile before breakdown to a wake-like profile after breakdown with axial distance [37].

The key of forming yarn for air-jet spinning is to produce sufficient leading-end free edge fibers, and form a larger twist difference between these fibers and yarn core. In accordance with our simulation, as the fiber strand passes through the twisting chamber, the weak opposite swirling

DOI: 10.1002/fld

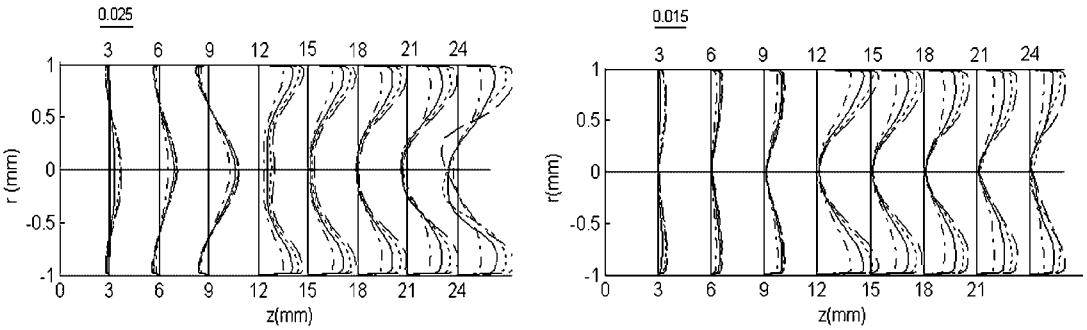

Figure 8. Velocity profiles at different pressures: left figure, axial velocity; and right figure, tangential velocity. Dash-dotted lines (-.), solid lines (-), dotted lines (:) and dashed lines (- -) represent pressures $P = 1.5, 2.0, 2.5$ and 3.0×10^5 Pa, respectively; the scaling of the shown quantities is given by the number in the upper left corner of the figure.

balloon near the upstream wall can delay the edge fiber end to be picked up by the core strand. It is helpful to form a larger twist difference. Some factors, such as the opposite winding of the spiral and the buffeting caused by the vortex breakdown, will help the edge fibers to loose wrapping and produce more wrapping fibers. Based on this reason, yarn tenacity can be improved.

3.3. Effect of nozzle pressure

Several researchers have used spinning experimental methods to study the influence of nozzle pressure [1–3] and the results show that it is the most important parameter affecting the mechanical properties of air-jet yarns. Because the radial velocity is very weak, Figure 8 only shows the tangential and axial velocities' profiles along radial direction at different z-axial positions for the different pressure $P = 1.5, 2.0, 2.5$ and 3.0×10^5 Pa cases. Firstly, for all cases, it is observed that the rules of velocity distributions are quite similar. At a low-pressure condition, velocity distributes are symmetrical and vortex breakdown in downstream of the injectors cannot occur because actual outlet pressure is close to external pressure. Secondly, as is expected, velocities increase with increasing nozzle pressure. However, the increase in velocity tends to decline as the pressure exceeds 2.5×10^5 Pa. It is clear from the figures that with pressure increase, the recirculation strength near the upstream wall increases and the location gradually shifts towards the nozzle inlet. Although the vortex breakdown location of the injector downstream is moved slightly downward with pressure increase, both its radial extent and buffeting intensity increase.

4. CONCLUSIONS

The 3D compressible swirl flow in the nozzle of air-jet spinning using the realizable k–ε turbulence model has been studied in the present work. Meanwhile, the effect of the nozzle pressure was also discussed. The following conclusions can be drawn after the detailed analysis:

1. Reverse flow appears near the wall and the weak opposite rotation balloon is formed in upstream of the injection due to compressible effects. A spiral-type vortex breakdown is also observed in downstream of the injectors.

DOI: 10.1002/fld

2. The flow structures show periodical behavior. Recirculation zone near the wall upstream of the injection shifts towards the nozzle inlet while the vortex breakdown slowly moves downstream during the whole transient period.
3. From the velocity profile, the maximum tangential velocity near the wall decreases as swirl decays. On the contrary, the maximum axial velocity increases with increase in axial distance. A flow-reversal region is found in the core in tangentially injected swirl flow. The area occupied by the flow-reversal region increases as the swirl intensity decreases. On the other hand, according to the tangential velocity distribution, a very small free-vortex zone is observed.
4. With increasing nozzle pressure, the velocity increases and vortex breakdown location is moved slightly downward, whereas the rule of the velocity distribution does not change. Note that vortex breakdown does not occur at lower nozzle pressure.

ACKNOWLEDGEMENTS

This work was supported by the Specialized Research Fund for the Doctoral Program of Higher Education (SRFDP) in China under grants No. 20040255009.

REFERENCES

1. Grosberg P, Oxenham W, Miao M. The insertion of 'twist' into yarns by means of air-jets, part 1: an experimental study of air-jet spinning. *Journal of the Textile Institute* 1987; **78**:189–203.
2. Chasmawala RJ, Hansen SM, Jayaraman S. Structure and properties of air-jet spun yarns. *Textile Research Journal* 1990; **60**:61–69.
3. Lawrence CA, Baqui MA. Effects of machine variables on the structure and properties of air-jet fasciated yarns. *Textile Research Journal* 1991; **61**:123–130.
4. Heuberger O, Ibrahim SM, Field FC. Technology of fasciated yarns. *Textile Research Journal* 1971; **41**:768–773.
5. Oxenham W, Basu A. Effect of jet design on the properties of air-jet spun yarns. *Textile Research Journal* 1993; **63**:674–678.
6. Zeng YC, Yu CW. Numerical simulation of air flow in the nozzle of an air-jet spinning machine. *Textile Research Journal* 2003; **73**(4):350–356.
7. Yu CW, Zhang WG. The distribution of airflow field in the nozzle of an air-jet spinning machine. *Journal of China Textile University* 1996; **22**(4):47–57.
8. Yowakim FM, Kind RJ. Mean flow and turbulence measurements of annular swirling flows. *Journal of Fluids Engineering* (ASME) 1988; **110**:257–263.
9. Nissan AH, Bresan VP. Swirling flow in cylinders. *AIChE Journal* 1961; **7**:543–547.
10. Ito S, Ogawa K, Kuroda C. Decay process of swirling flow in a pipe. *International Chemical Engineering* 1979; **19**:600–605.
11. Chang F, Dhir VK. Turbulent flow field in tangentially injected swirl flows in tubes. *International Journal of Heat and Fluid Flow* 1994; **15**(5):346–356.
12. Yajnik KS, Subbsish MV. Experiments on swirling turbulent flows. Part 1. Similarity in swirling flows. *Journal of Fluid Mechanics* 1973; **60**:665–687.
13. Kitoh O. Experimental study of turbulent swirling flow in a straight pipe. *Journal of Fluid Mechanics* 1991; **225**:445–479.
14. Bottaro A, Ryhming IL, Wehrli MB, Rys ES, Rys P. Laminar swirling flow and vortex breakdown in a pipe. *Computer Methods in Applied Mechanics and Engineering* 1991; **89**:41–57.
15. Chen J, Haynes BS, Fletcher DF. A numerical and experimental study of tangentially injected swirling pipe flows. *Second International Conference on CFD in the Minerals and Process Industries CSIRO*, Melbourne, Australia, 6–8 December 1999; 485–490.
16. Kobayashi T, Yoda M. Modified k–ε model for turbulent swirling flow in a straight pipe. *JSME International Journal* 1987; **30**:66–71.
17. Najafi AF, Saidi MH, Angilella JR, Sadeghipour MS, Souhar M. Turbulence modeling in a swirling decay pipe flow. *Second BSME–ASME International Conference on Thermal Engineering*, Dhaka, 2004.

DOI: 10.1002/fld

18. Favre A. Statistical equations of turbulent gases. *Problems of Hydrodynamics and Continuum Mechanics*. SIAM: Philadelphia, PA, 1969; 231–266.
19. Sloan DG, Smith PJ, Smoot LD. Modeling of swirl in turbulent flow systems. *Progress in Energy and Combustion Science* 1986; **12**(3):163–250.
20. Nallasamy M. Turbulence models and their applications to the prediction of internal flows: a review. *Computers and Fluids* 1987; **15**(2):151–194.
21. Favaloro SC, Nejad AS, Ahmed SA. Experimental and computational investigation of isothermal swirling flow in an axisymmetric dump combustor. *Journal of Propulsion and Power* 1991; **7**(3):348–356.
22. Jones WP, Pascau A. Calculation of confined swirling flows with a second moment closure. *Journal of Fluids Engineering*, *Transactions of the ASME* 1989; **111**(3):248–255.
23. Mondal S, Datta A, Sarkar A. Influence of side wall expansion angle and swirl generator on flow pattern in a model combustor calculated with k–ε model. *International Journal of Thermal Sciences* 2004; **43**:901–914.
24. Bradshaw P. Effects of streamline curvature on turbulent flows. *AGARDograph Report No.169*, 1973.
25. Shih TH, Liou WW, Shabbir A, Zhu J. A new k–ε Eddy-viscosity model for high Reynolds number turbulent flows. *Computers and Fluids* 1995; **24**(3):227–238.
26. Kim SE, Choudhury D, Patel B. Computations of complex turbulent flows using the commercial code FLUENT. *Proceedings of the ICASE/LaRC/AFOSR Symposium on Modeling Complex Turbulent Flows*, Hampton, VA, 1997.
27. Kucukgokoglan S, Aroussi A, Pickering SJ. Prediction of interactions between burners in multi-burner systems. *International Symposium on Multiphase Flow and Transport Phenomena*, Antalya, 2000.
28. Reynolds WC. *Fundamentals of Turbulence for Turbulence Modeling and Simulation*. Lecture Notes for Von Karman Institute. *Agard Report No. 755*, NATO, New York, 1987.
29. Leonard BP. A stable and accurate convective modelling procedure based on quadratic upstream interpolation. *Computer Methods in Applied Mechanics and Engineering* 1979; **19**:59–98.
30. Brandt A. Algebraic multigrid theory: the symmetric case. *Applied Mathematics and Computation* 1986; **19**:23–56.
31. Stüben K. Algebraic multigrid (AMG): experiences and comparisons. *Applied Mathematics and Computation* 1983; **13**:419–452.
32. Webster R. An algebraic multigrid solver for Navier–Stokes problems. *International Journal for Numerical Methods in Fluids* 1994; **18**(6):761–780.
33. Chang Q, Wong YS, Fu H. On the algebraic multigrid method. *Journal of Computational Physics* 1996; **125**: 279–292.
34. Stüben K. A review of algebraic multigrid. *Journal of Computational and Applied Mathematics* 2001; **128**: 281–309.
35. Brücker C. Study of vortex breakdown by particle tracking velocimetry. Part 2: spiral-type vortex breakdown. *Experiments in Fluids* 1993; **14**:133–139.
36. Krause HW. Staple fibre spinning systems. *Journal of the Textile Institute* 1985; **76**(3):185–195.
37. Leibovich S. The structure of vortex breakdown. *Annual Review of Fluid Mechanics* 1978; **10**:221–246.
38. Gupta A, Lilley DG, Syred N. *Swirl Flow*. Energy and Engineering Sciences Series. Abacus Press: Tunbridge Wells, U.K., 1984.

DOI: 10.1002/fld